Modeling & Calibration of an Ad-Hoc Circular Array for Adaptive Direction Finding

Logan Satterfield[1], Jonathan Owen[1], Christian Jones[2], Alex Bouvy[3], Benjamin Kirk[3], Shannon Blunt[1]
[1] Radar Systems Lab, University of Kansas, Lawrence, KS
[2] Naval Research Laboratory, Washington, D.C.
[3] DEVCOM Army Research Laboratory, Adelphi, MD

***Abstract*— While various adaptive beamforming methods exist in the literature, there is a clear dearth of experimental demonstrations in hardware. Here, modeling and calibration techniques are introduced to enable adaptive direction finding via the reiterative super-resolution (RISR) algorithm on a low-cost, ad hoc uniform circular array (UCA). Due to the nonuniform structure of the UCA (in Cartesian space), additional physical array considerations must be incorporated into the signal model such as element-level beam patterns and phase center positions. Using this array and associated hardware, the RISR algorithm is successfully demonstrated to achieve super-resolution with precise estimates having an average angular error of 1.3° and worst-case error of 4.3°. Practical calibration aspects are also examined.**

Antenna elements are modeled via electromagnetic simulation to approximate gain and phase responses. Element phase centers are estimated to coincide with the resonant dipole of the log-periodic dipole antenna (LPDA) at the chosen center frequency, subsequently impacting the modeled array factor. The element beampattern is realized via the MATLAB Antenna Toolbox to inform the gain/phase of the anticipated UCA steering matrix. The amended steering matrix is applied during array calibration, which leverages a variant of the Wiener formulation to generate a channel equalization filter bank. Other adaptive direction finding algorithms including minimum variance distortionless response (MVDR) and multiple signal classification (MUSIC) are applied to the calibrated data for comparison.

Keywords—uniform circular array (UCA), array calibration, direction finding

I. Introduction

The UCA provides a simple array geometry to achieve 360° direction finding (DF). However, the array manifold is more complex than a uniform linear array (ULA) with the same number of elements due to the expanded field of view. Specifically, the ULA often treats the effects of individual elemental beampatterns as negligible (when sufficiently broad beam) because steering occurs within the 3dB beamwidth of all elements – thus magnitude and phase variations across elements are insignificant within the main-beam for a given look direction. Precise phase center coordinates are similarly less impactful to ULAs, so long as antenna elements are oriented similarly and the inter-element spacing is known. Indeed, ULAs reap considerable benefits from the implied Vandermonde (or nearly so) steering matrix, allowing for computational improvements via fast Fourier transform (FFT) or chirp-Z transform (CZT) [1]. Calibration of a UCA with radially pointed elements is considerably more challenging due to varying per-element look angles, non-uniform phase center locations on the *x*-*y* azimuthal plane, and phase center displacement as a function of frequency.

Many prior UCA calibration methods [2]-[5] utilize a phase mode (or beam-space) transform [6] to construct a virtual ULA (VULA) that approximates Vandermonde form. However, this transformed array manifold may introduce error, particularly when constructed from a relatively small number of elements [7]. Other methods require a dedicated calibration antenna element as part of the array [8],[9].

The calibration method applied here is a variation of the Wiener filter formulation [10] performed in element-space and relies on a small set of training signals from known incident angles to generate equalization filters for all channels to perform DF calibration. Each antenna element has an identical model and (omitting manufacturing variances) exhibits a fixed spatial response, which is then displaced/rotated to the respective positions and look-directions of the UCA elements. To acquire the gain/phase response of each antenna at a given operating frequency for system modeling, a simplified antenna model is developed via the MATLAB Antenna Toolbox, allowing for simulated changes in center frequency or angular resolution without requiring prior generation of measured lookup tables in a controlled anechoic setting. Importantly, open-air calibration is demonstrated using an ad hoc array configuration and coarse hand measurements to achieve fine angle estimation. Applying the spatial RISR algorithm after calibration demonstrates precise and accurate estimation. Comparisons are made to the MVDR and MUSIC algorithms on the same UCA platform.

II. Physical Steering Matrix Model

Consider the array factor for an arbitrary array geometry as

$$\mathrm{AF}(\theta,\phi) = \sum_{n} u_n \mathrm{e}^{\,\mathrm{j}\mathbf{c}_n^T\mathbf{k}(\theta,\phi)}, \tag{1}$$

where u_n is the weight of the n^{th} antenna element (of N), and θ,ϕ are elevation and azimuth angles, respectively. Given a narrowband spectrum assumption, the wave number (or K-space) spherical-to-Cartesian transform vector in (1) is

$$\mathbf{k}(\theta,\phi) = \tfrac{2\pi}{\lambda}\begin{bmatrix}\sin\phi\cos\theta\\ \cos\phi\cos\theta\\ \sin\theta\end{bmatrix}, \tag{2}$$

for λ the center frequency's wavelength and Cartesian coordinates of the n^{th} antenna element denoted by

This work was supported by a subcontract with HII for research sponsored by DEVCOM Army Research Laboratory under prime contract #FA8075-18-D-0002.
DISTRIBUTION STATEMENT A. Approved for public release.

$$\mathbf{c}_n = \begin{bmatrix} x_n \\ y_n \\ z_n \end{bmatrix}. \quad (3)$$

Setting $z_n = 0$ (for a UCA on the x-y plane), the steering vector for a signal arriving from angles θ, ϕ is represented by

$$\bar{\mathbf{s}}(\theta, \phi) = e^{j\mathbf{C}^T\mathbf{k}(\theta,\phi)} \quad (4)$$

where $\mathbf{C} = [\mathbf{c}_1, \cdots, \mathbf{c}_N]$ is the matrix of Cartesian array positions. For a discretization of M look-angles of interest (with $M \gg N$), the steering vectors $\bar{\mathbf{s}}(\theta, \phi)$ are collected into the columns of the $N \times M$ steering matrix

$$\bar{\mathbf{S}} = [\bar{\mathbf{s}}(\theta_1, \phi_1) \quad \bar{\mathbf{s}}(\theta_2, \phi_2) \quad \cdots \quad \bar{\mathbf{s}}(\theta_M, \phi_M)]. \quad (5)$$

Herein, the steering matrix $\bar{\mathbf{S}}$ is discretized across all azimuth via M equally spaced angles ϕ_m at a fixed elevation $\theta = 0°$. The steering matrix is further impacted by the dissimilar antenna beampatterns composing the UCA. The WA5VJB 2-11 GHz log-periodic dipole array (LPDA) antenna depicted in Fig. 1 was chosen due to its reasonable wideband performance, low cost, and availability. It is necessary to include a model of the element beampattern during array processing as a steering matrix modifier. To accomplish this, the simulated antenna model shown in Fig. 2 was obtained using hand measurements and utilizing the MATLAB Antenna Toolbox. The operating center frequency is $f_c = 3.425$ GHz.

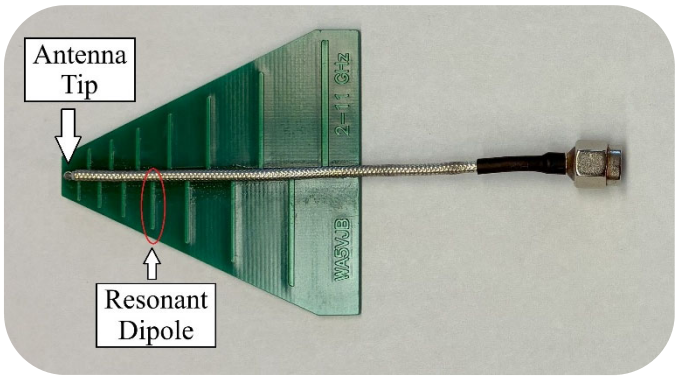

Fig. 1. WA5VJB 2-11 GHz LPDA antenna element. Note the antenna tip (used to reference phase center position) and the dipole that is approximated to be nearest to the true phase center of the antenna at 3.425 GHz.

The ensuing model is used to simulate the element beampattern $g(\theta, \phi, \hat{\theta}, \hat{\phi})$, with the peak gain centered at elevation $\hat{\theta}$ and azimuth $\hat{\phi}$. The element beampattern is sampled across all azimuth for M equally spaced angles ϕ_m at a fixed elevation $\theta = 0°$, creating the $M \times 1$ beampattern cut $\mathbf{g}(\hat{\theta} = 0°, \hat{\phi} = 0°)$ shown in Fig. 3. The azimuth indices shown correspond to the same angles selected to construct the steering matrix $\bar{\mathbf{S}}$. Because the individual array elements are pointing in different directions that consequently vary $\hat{\phi}_n$, the beampattern $\mathbf{g}(\hat{\theta} = 0°, \hat{\phi} = 0°)$ must be transformed to reflect the respective orientations of all n antennas.

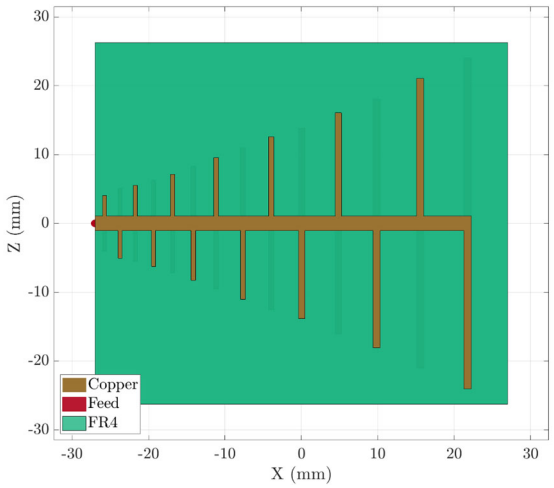

Fig. 2. Simulated LPDA antenna element, created with the MATLAB Antenna Toolbox.

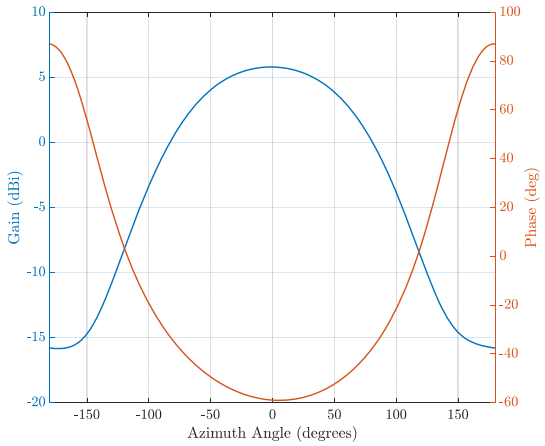

Fig. 3. Azimuth gain and phase cuts of the simulated antenna element at 3.425 GHz, defining $\mathbf{g}(\hat{\theta} = 0°, \hat{\phi} = 0°)$.

The transformation from $\mathbf{g}(\hat{\theta} = 0°, \hat{\phi} = 0°)$ to $\mathbf{g}(\hat{\theta} = 0°, \hat{\phi}_n)$ is accomplished via linear interpolation to translate the beampattern to an azimuth grid that is spatially offset to $\hat{\phi}_n$. The set of spatially-offset beampatterns then modifies the steering matrix from (5) via element-wise multiplication $\odot$ as

$$\mathbf{S} = \bar{\mathbf{S}} \odot \begin{bmatrix} \mathbf{g}^T(\hat{\theta} = 0°, \hat{\phi}_1) \\ \mathbf{g}^T(\hat{\theta} = 0°, \hat{\phi}_2) \\ \vdots \\ \mathbf{g}^T(\hat{\theta} = 0°, \hat{\phi}_N) \end{bmatrix} \quad (6)$$

to form a steering matrix $\mathbf{S}$ with beampatterns incorporated.

III. Wiener Filter Calibration

The calibration aims to form a channel-equalization filter that makes all channels have the same spectral response, while also compensating the phase weights from (6). Because a variety of errors are anticipated due to array uncertainty, Q distinct calibration angles are considered and subsequent averaging reduces error. A simple approach to form the channel-equalization filter is through the standard Wiener filter (WF)

formulation that minimizes mean squared error (MSE) [10]. The typical form solves the objective function

$$J(\mathbf{w}) = E[e^2[\ell]] = E[(d[\ell] - \mathbf{w}^H\mathbf{y}[\ell])^2], \tag{7}$$

where $\mathbf{w}$ is the equalization filter, $d[\ell]$ is the desired response of the incoming signal, and $\mathbf{y}[\ell]$ is the measured data. The well-known WF closed-form solution is

$$\mathbf{w} = E[\mathbf{y}[\ell]\mathbf{y}[\ell]^H]^{-1}E\big[d^*[\ell]\mathbf{y}[\ell]\big], \tag{8}$$

where $E[\mathbf{y}[\ell]\mathbf{y}[\ell]^H]$ is approximated via the sample covariance matrix (SCM) $\mathbf{R}$ and $E\big[d^*[\ell]\mathbf{y}[\ell]\big]$ is approximated via the sample cross-correlation vector $\mathbf{p}$.

Let array data $\mathbf{Y}$ consist of $N \times L$ element/time samples based on a single incoming incident signal from azimuth direction ϕ_q (of Q calibration trials). The beampattern-incorporated steering vector from (6) for the direction ϕ_q is denoted as $\mathbf{s}\left(\theta = 0°, \phi_q\right)$. From the matched beamforming estimate in the incoming direction $\mathbf{d}^T = \mathbf{s}^H\left(\theta = 0°, \phi_q\right)\mathbf{Y}$, an estimate of the $L \times 1$ desired signal $\mathbf{d}$ may be determined to within some array uncertainty error. Alternatively, if the receive data is time-sample aligned with the captured calibration signal, then $\mathbf{d}$ is strictly known and improves subsequent calibration.

Each row of $\mathbf{Y}$ represents the L time samples on a given channel denoted as $\mathbf{y}_n$ for the n^{th} antenna element. The SCM for a single channel, which corresponds to forming a K tap WF (with $K = 25$ selected for full channel characterization), is determined as

$$\mathbf{R}_n = \left(\frac{1}{L-K+1}\right)\mathbf{T}_n\mathbf{T}_n^H. \tag{9}$$

The $K \times (L-K+1)$ Toeplitz matrix $\mathbf{T}_n$ is composed of receive time snapshots along its columns as

$$\mathbf{T}_n = \begin{bmatrix} y(K) & y(K+1) & \cdots & y(L) \\ \vdots & \vdots & \ddots & \vdots \\ y(1) & y(2) & \cdots & y(L-K+1) \end{bmatrix}. \tag{10}$$

The cross-correlation vector $\mathbf{p}_n$ is defined between the time aligned desired response $\tilde{\mathbf{d}}$ (obtained by removing the first K samples of $\mathbf{d}$) and receive data snapshot matrix $\mathbf{T}_n$ determined via

$$\mathbf{p}_n = \left(\frac{1}{L-K+1}\right)\mathbf{T}_n\tilde{\mathbf{d}}^* . \tag{11}$$

The WF for any single channel is thus formed as

$$\mathbf{w}_n = \mathbf{R}_n^{-1}\mathbf{p}_n. \tag{12}$$

The filters determined across all N element channels subsequently comprise the filter bank

$$\mathbf{W} = [\mathbf{w}_1 \quad \mathbf{w}_2 \quad \ldots \quad \mathbf{w}_N]. \tag{13}$$

Denoting (12) as $\mathbf{W}_q$ for the q^{th} of Q distinct calibration angles, the different filter banks can be averaged to get the single $K \times N$ channel equalization filter bank

$$\mathbf{W}_{\text{eq}} = \frac{1}{Q}\sum_{q=1}^{Q}\mathbf{W}_q \odot \left(\mathbf{1}_{K\times 1} \cdot \mathbf{s}\left(\theta = 0°, \phi_q\right)^T\right). \tag{14}$$

Reincorporation of the steering vector in (14) removes phase dependence for varying calibration directions ϕ_q, such that averaging does not inflict decoherence. With increasing test angles, assuming similar error tolerances, uncertainty should reduce via averaging. Each n^{th} channel equalizer that composes $\mathbf{W}_{\text{eq}}^*$ then filters each respective incoming data stream of $\mathbf{Y}$ via convolution. Variations of this algorithm can also reduce noise gain via methods such as [11].

IV. Array Configuration

To test over-the-air performance of the modeling and calibration routines, an 8-element UCA was constructed using WA5VJB LPDA elements. The elements are mounted on a circular bracket with modest positional uncertainty due to imperfect array construction. Additionally, due to the wideband nature of LPDA antennas, the phase center varies significantly with frequency such that it must be accounted for to produce an accurate array manifold for a given operating frequency.

The phase center position is approximated to coincide with the dipole closest to electrical length $\lambda/2$ for the given operating frequency and dielectric medium. For an operating frequency of 3.425 GHz in an FR4 dielectric with $\epsilon_r \approx 4$ and $\mu_r \approx 1$, for $\lambda = c/(f\sqrt{\epsilon_r\mu_r})$ [12], we determine $\lambda/2$ to be 22 mm. This places the phase center near the 7^{th} smallest dipole, approximately 20 mm behind the antenna tip in Fig. 1. For the UCA geometry, this results in an adjacent phase center to phase center spacing of 96 mm (or 1.1λ) as shown in Fig. 5.

This calculation is corroborated with another publication using the same antenna at a similar operating frequency [13], which found the phase center to be approximately 22 mm behind the tip at an operating frequency of 3.456 GHz. The UCA inter-element spacing is thus assumed to be 96 mm, which then maps the 8 element positions from circular to Cartesian coordinates x_n and y_n for use in (3). As seen in Fig. 6, this array pattern results in quite high peak sidelobe level (PSL) of -4 dB, but does allow for 360° coverage. These sidelobes are significant due to the undersampled array (1.1λ spacing), but are not entirely ambiguous (i.e. grating lobes) because the circular array is non-uniform in a Cartesian space. Note that antenna flex may inflict additional error in the assumed phase center positions $\mathbf{c}_n$.

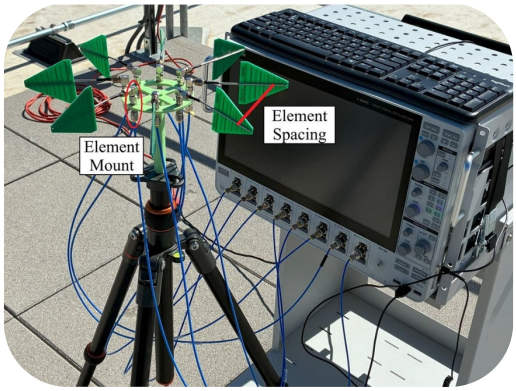

Fig. 4. 8-Element UCA connected to multi-channel oscilloscope.

V. Experiment Setup

The array elements are connected to a Tektronix MSO68B oscilloscope for data capture. A separate arbitrary waveform generator (AWG) generates an LFM signal with a center frequency of 3.425 GHz, bandwidth of 50 MHz, and a waveform repetition interval of 2 μs at 100% duty cycle. The calibration signal LFM is amplified and transmitted towards the array from a given angle and data is captured with the oscilloscope. The process is repeated for multiple incident angles spanning the full azimuthal space around the array.

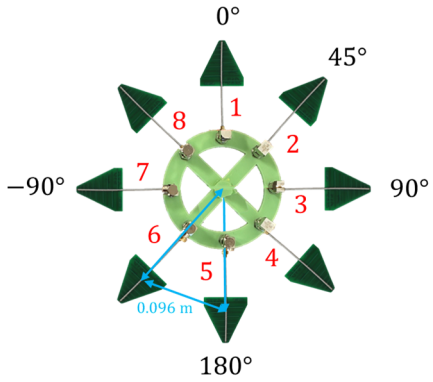

Fig. 5. Illustration of 8-Element UCA overhead view with defined angular orientations. Antennas are vertically oriented.

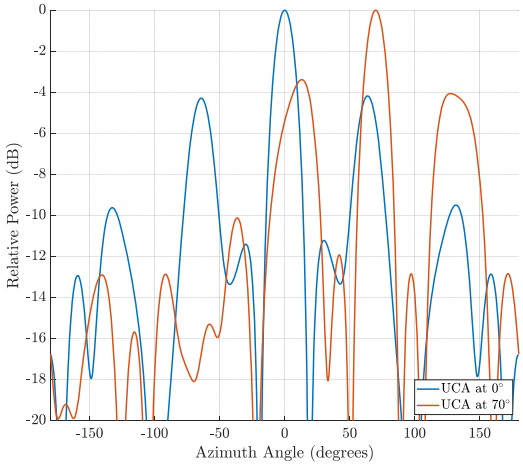

Fig. 6. Simulated beampattern for the experimental UCA, operating at 3.425 GHz, steered to either azimuth $\phi = 0°$ or 70° for elevation $\theta = 0°$.

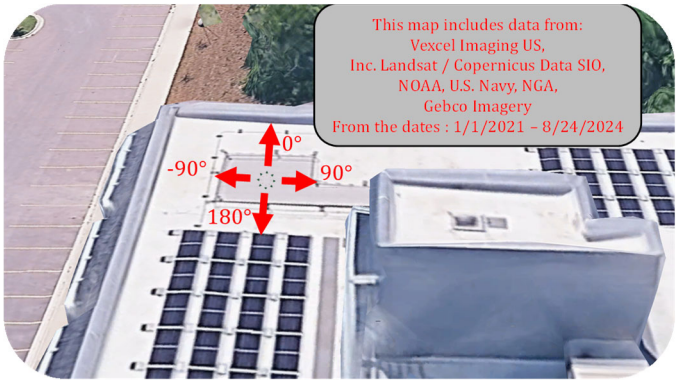

Fig. 7. Orientation of UCA during open-air experiment.

A subset of the captures are used to generate/train the calibration filters, and another subset (encompassing the first) is used to analyze/validate the results. While effort is made to record the incident angle as accurately as possible with a yard stick, no advanced measurement methods are used (i.e. GPS) and thus, the results are inherently constrained by human error. Qualitative estimates place the positional uncertainty at approximately ±2°, though exact isolation of error introduced by human versus algorithmic contributions would require a fine-tuned positioning method. Results within or near that threshold are not likely to be directly indicative of calibration performance and will require further investigation with more precise positional and angular measurements. Refinement of angular error can feasibly be achieved during online angle estimation via adaptation to unknown signals [14].

To analyze the effectiveness of the calibration routine, we perform both adaptive and non-adaptive DF on the calibrated data. LFM signals incident at 0°, 90°, 180°, and -90° are used to generate/train the calibration filter. Then, sixteen LFM signals, incident at uniformly-spaced angles around the array in 22.5° increments are used to test/validate the calibration. Of course, this approach implies the error at angles used for training will be reduced in comparison to the remainder during validation. The calibration and accuracy assessment are evaluated within the same multipath environment. Performance will degrade if the array is moved to a different location without recalibration.

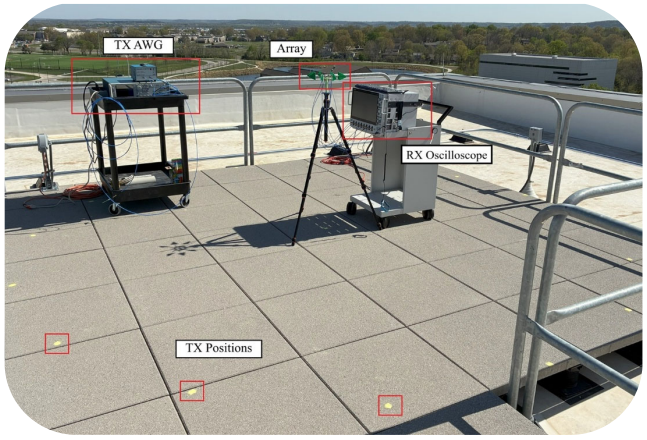

Fig. 8. Open-air test setup

VI. Direction Finding Results

The signals are processed with a spatial matched beamformer (MB), MVDR [15], MUSIC [16], and RISR [17], with each evaluated for angular estimate error and peak sidelobe level (PSL) under controlled conditions. MVDR and MUSIC are performed on 100 temporal snapshots to estimate the spatial covariance they require, while RISR can feasibly be performed on a single snapshot due to its structured covariance matrix [17]. However, by using noncoherent averaging during angle estimation RISR DF may be improved [17]. Hence, 25 temporal snapshots are noncoherently averaged assuming modest spatial stationarity. For spatial signal estimation, a slight degree of stationarity may be assumed while still achieving adequate performance, even in non-stationary scenarios [18]. For the MUSIC algorithm, the noise and signal subspaces are separated with a threshold at 1% of the largest eigenvalue's power. A partially gain-constrained formulation of RISR is applied, here

with $\alpha = 0.65$, allowing for both super-resolution and accurate power estimation [19]. The signal-to-noise ratio (SNR) for all incoming angles is 30 dB for fair comparison, although RISR has been shown to perform well even with SNRs below 10 dB [19]. High SNR signals are evaluated to characterize algorithmic error, although performance does degrade with reduced SNR.

For each incident angle, in combination with each algorithm, a time series of snapshots is processed and the first and second largest local maxima peaks are recorded. The power difference between the two largest local maxima peaks is recorded as the PSL. The deviation between the true (hand-measured) incident angle and the "center of mass" of the highest power beam is recorded as the angular error. The angular center of mass is calculated as

$$\phi_{\text{est}} = \phi_{\text{peak}} + \frac{\sum_{i \in B_{\text{null}}} \hat{x}_i i}{\sum_{i \in B_{\text{null}}} \hat{x}_i}, \tag{15}$$

where $\hat{x}_i$ is the angle estimate at the i^{th} angle index (in relation to the peak, where $i = 0$) and ϕ_{peak} is the angle corresponding to the peak response. The B_{null} term is the set of indices within the null-to-null beamwidth after super-resolution, found via local minima search, as each algorithm realizes different degrees of super-resolution.

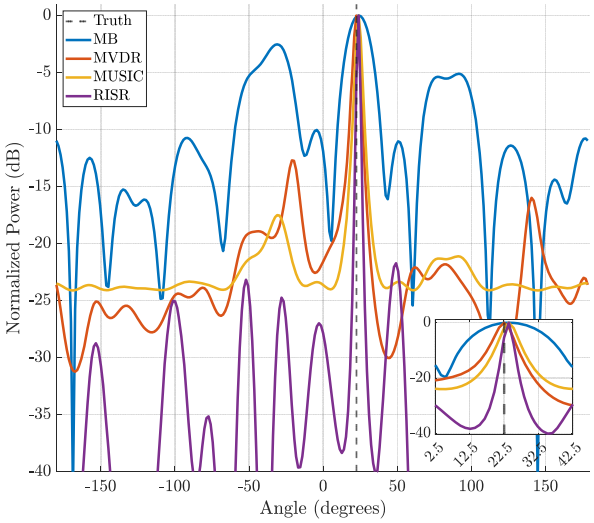

Fig. 9. Experimental, calibrated DF response of a signal incident at 22.5° azimuth for a single time instant, processed with MB, MVDR, MUSIC, and RISR. Inset shows the same data, zoomed in around 22.5°.

Fig. 9 shows a DF estimate of the signal incident at 22.5° for a single time instant, processed with all algorithms. The MB output has high sidelobes due to the spatially undersampled and non-uniform element spacing of the array (per Fig. 6). The adaptive DF algorithms all perform well, achieving a reasonable degree of super-resolution. That said, RISR achieves nearly 2× finer super-resolution while using only 25% of the temporal snapshots compared to MVDR and MUSIC. All three adaptive algorithms have their highest sidelobe between -13 and -21 dB (at or near the MB sidelobe locations), with MUSIC having a flatter spatial spectrum and RISR having lower average sidelobes than the other two algorithms.

Fig. 10 extends the analysis across multiple time snapshots, showing the average angular deviation for each time series of snapshots, over all validation angles. The data is grouped by incident angle and each color corresponds to a particular algorithm (same as in Fig. 9). All algorithms have a median error of less than 1.3° when computed across the entire angular space. Angular error outliers could be due to antenna misalignment in the corresponding array section, human error in the transmit positioning, or a nonideal calibration dataset.

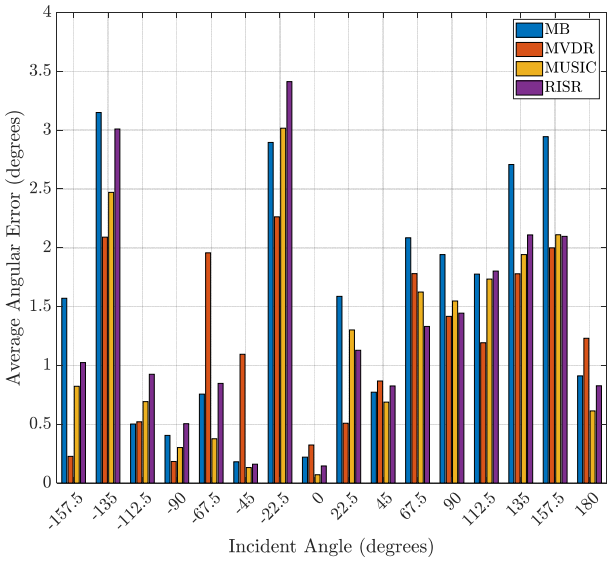

Fig. 10. Mean angular error in degrees (averaged across time), grouped by angle for each algorithm.

Additionally, at -45° and -67.5°, the mean error for MVDR is significantly higher than the other algorithms – implying an algorithmically driven source of error. Finally, the higher-than-average deviation for all 4 methods at -22.5° and -135° indicates that the positional errors of the calibration signals are likely to be higher than for the other test angles. Indeed, angular error within an offline calibration routine is sensitive to the positional manufacturing tolerance of the whole array and the incoming calibration signal certainty, further suggesting that for ad hoc arrays an online calibration is necessary, albeit at the price of a somewhat higher computational cost. If precise positioning is determinable during field testing via GPS or otherwise, the proposed calibration routine could conceivably compensate for non-ideal environmental effects such as multipath, which can only otherwise be avoided via anechoic measurements.

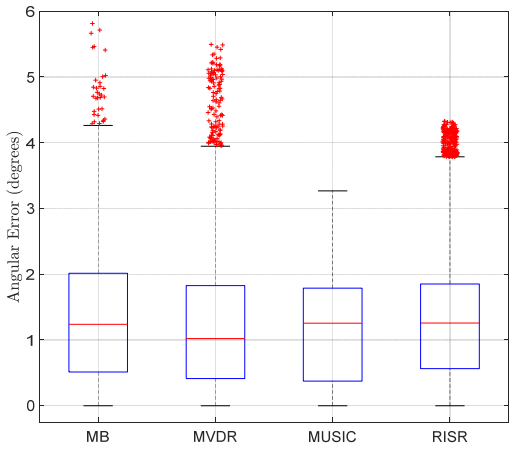

Fig. 11. Angular error boxplots across time/angle for each algorithm. Outliers are pictured as red marks.

Fig. 11 is calculated from the same angular error data as shown in Fig. 10, with data grouped by algorithm to give a sense of average performance across azimuthal space. The boxplots show that all algorithms have similar error distributions. All algorithms exhibit similar first, second, and third quartile performance, although MB, MVDR, and RISR all exhibit outliers. The worst case angular error (including outliers) for each algorithm are 5.8°, 5.5°, 3.3°, and 4.3° for MB, MVDR, MUSIC, and RISR, respectively. However, the presence of additional incoming signals would likely impact error analysis. Of course, a clear pitfall of MUSIC occurs when more than one incoming signal is present across space, then requiring rank estimation to determine the exact number of incoming signals [10]. Incorrect rank estimation would result in significantly degraded estimation. Additionally, RISR is representative of single snapshot beamforming methods, achieving comparable average angular error to MUSIC with fewer time snapshots.

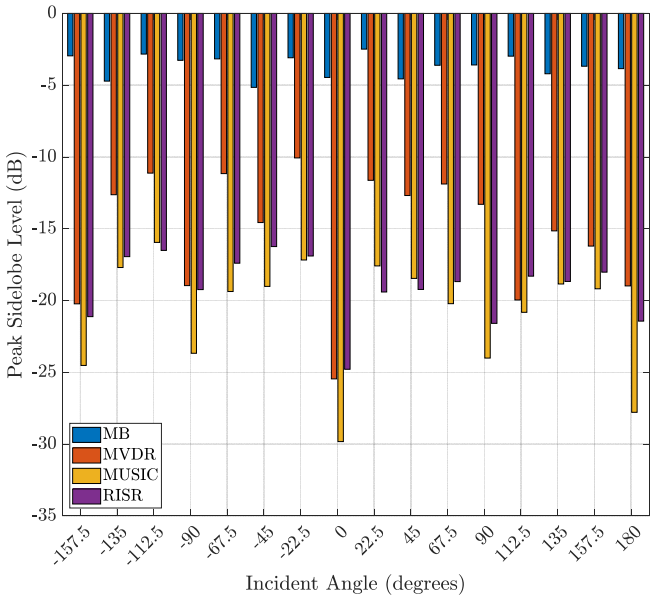

Fig. 12. Mean peak sidelobe level (PSL) across time. Results for each time series of processed data are shown, grouped by angle with different colors for each algorithm. Lower PSL values indicate better performance.

As seen in Fig. 12, each algorithm achieves self-consistent peak sidelobe levels across the azimuthal space, with PSL values reduced at calibration training angles. RISR and MUSIC achieve comparable PSL across azimuth, with MUSIC slightly outperforming RISR in this single signal scenario.

VII. Conclusions

The experimental modeling and calibration process achieves low angular error using a relatively small number of reference calibration signals. Because the calibration filter and antenna model may be generated prior to performing DF, the increase in in-situ processing time is small, requiring only a filtering operation and modified steering matrix. Further extension of the experimental test to include multiple incoming signals would provide insight into how the array and calibration routines perform in combination with adaptive algorithms in more demanding environments (i.e. multiple nonstationary signals).

References

[1] L. Rabiner, R. Schafer, C. Rader, “The chirp Z-transform algorithm and its application,” *The Bell System Technical Journal*, vol. 48, no. 5, June 1969.

[2] M. Wax, J. Sheinvald, "Direction finding of coherent signals via spatial smoothing for uniform circular arrays," *IEEE Trans. on Antennas and Propagation*, vol. 42, no. 5, pp. 613-620, May 1994.

[3] K. Adhikari, R. Al Kinani, “Transformation of a circular array to a linear array with a Vandermonde structure,” *Digital Signal Processing*, vol. 140, Aug. 2023.

[4] M. Boddi, M. Rosamilia, A. Aubry, A. De Maio, " Iterative calibration and direction-of-arrival estimation for uniform circular arrays affected by mutual coupling," *IEEE Sensors Letters*, vol. 8, no. 6, pp. 1-4, June 2024.

[5] C.P. Mathews, M.D. Zoltowski, "Eigenstructure techniques for 2-D angle estimation with uniform circular arrays," *IEEE Trans. Signal Processing*, vol. 42, no. 9, pp. 2395-2407, Sept. 1994.

[6] D. Davies, “A transformation between the phasing techniques required for linear and circular aerial arrays,” *Proc. Inst. Electr. Eng.*, vol. 112, no. 4, pp. 2041–2045, Nov. 1965.

[7] F. Belloni, V. Koivunen, "Beamspace transform for UCA: error analysis and bias reduction," *IEEE Trans. Signal Processing*, vol. 54, no. 8, pp. 3078-3089, Aug. 2006.

[8] T. Ouyang, L. Qian, L. Ding, F. Yang, "Mutual coupling calibration for uniform circular array using a single source," *International Conference on Wireless Comms. and Sig. Processing*, Hefei, China, Oct. 2014.

[9] T. Li, F.-S. Zhang, F. Zhang, Y.-L. Yao, L. Jiang, "Wideband and high-gain uniform circular array with calibration element for smart antenna application," *IEEE Antennas & Wireless Propagation Letters*, vol. 15, pp. 230-233, June 2016.

[10] S. Haykin, *Adaptive Filter Theory*, 5th Ed., Pearson, 2013.

[11] H. Cox, R. Zeskind, M. Owen, "Robust adaptive beamforming," *IEEE Trans. Acoustics, Speech, and Signal Processing*, vol. 35, no. 10, pp. 1365-1376, Oct. 1987.

[12] W. Hayt, *Engineering Electromagnetics*, 5th Ed., McGraw-Hill, 1989.

[13] P. Wade, “The WA5VJB LPA antenna as a multi-band dish feed,” 2004. https://www.w1ghz.org/antbook/conf/WA5VJB_LPA_feed.pdf

[14] C. C. Jones, *et al*., "Development and experimental assessment of robust direction finding and self-calibration," *IEEE Radar Conference*, New York City, NY, Mar. 2022.

[15] J. Capon, "High-resolution frequency-wavenumber spectrum analysis," *Proceedings of the IEEE*, vol. 57, no. 8, pp. 1408-1418, Aug. 1969.

[16] R. Schmidt, "Multiple emitter location and signal parameter estimation," *IEEE Transactions on Antennas and Propagation*, vol. 34, no. 3, pp. 276-280, March 1986.

[17] S.D. Blunt, T. Chan, K. Gerlach, "Robust DOA estimation: the reiterative superresolution (RISR) algorithm," *IEEE Trans. Aerospace & Electronic Systems*, vol. 47, no. 1, pp. 332-346, Jan. 2011.

[18] L. Satterfield, J. Owen, A. Bouvy, B. Kirk, P. McCormick, S. Blunt, "Reiterative MMSE using feed-forward prior estimates for improved direction finding," *IEEE Intl. Radar Conf.*, Atlanta, GA, May 2025.

[19] E. Hornberger, S.D. Blunt, T. Higgins, "Partially constrained adaptive beamforming for super-resolution at low SNR," *IEEE Intl. Workshop on Computational Advances in Multi-Sensor Adaptive Processing*, Cancun, Mexico, Dec. 2015.